EUROFUSION WPPFC-PR(16) 14700

A Hakola et al.

ERO and PIC simulations of gross and net erosion of tungsten in the outer strike-point region of ASDEX Upgrade

Preprint of Paper to be submitted for publication in
22nd International Conference on Plasma Surface Interactions
in Controlled Fusion Devices (22nd PSI)

This work has been carried out within the framework of the EUROfusion Consortium and has received funding from the Euratom research and training programme 2014-2018 under grant agreement No 633053. The views and opinions expressed herein do not necessarily reflect those of the European Commission.

ERO and PIC simulations of gross and net erosion of tungsten in the outer strike-point region of ASDEX Upgrade

A. Hakola[a,*], M. I. Airila[a], N. Mellet[b], M. Groth[c], J. Karhunen[c], T. Kurki-Suonio[c], T. Makkonen[c], H. Sillanpää[c],G. Meisl[d], M. Oberkofler[d], ASDEX Upgrade Team

[a]*VTT Technical Research Center of Finland Ltd., P. O. Box 1000, 02044 VTT, Finland*
[b]*CNRS, Aix-Marseille Université, PIIM, UMR 7345, 13397 Marseille, France*
[c]*Aalto University, Department of Applied Physics, P. O. Box 11100, 00076 Aalto, Finland*
[d]*Max Planck Institute for Plasma Physics, Boltzmannstr. 2, 85748 Garching, Germany*

Abstract

We have modelled net and gross erosion of W in low-density L-mode plasmas in the outer strike point of AUG by ERO and Particle-in-Cell (PIC) simulations. The strong net-erosion peak at the strike point was explained by the presence of light impurities in the plasma while the noticeable deposition peaks poloidally on both sides of the strike point could be attributed to the strong **E**×**B** drift, which affects the transport of particles along the target surfaces. In addition, simulations with weak cross-field diffusion corresponded most closely to the measured deposition profiles. The simulations indicate net/gross erosion ratio of 0.2-0.6, clearly smaller than the experimental value of ~0.6-0.7. The discrepancy is attributed to the measured profiles showing the outcomes of multiple erosion-deposition cycles.

Keywords: ASDEX Upgrade, Gross erosion, Net erosion, Tungsten, ERO modelling, PIC simulations, Particle drifts

**Corresponding author address*: VTT, P. O. Box 1000, 02044 VTT, Finland
**Corresponding author e-mail*: antti.hakola@vtt.fi

1. Introduction

The limited lifetime of plasma-facing components (PFCs) can be a potential showstopper in future fusion reactors including ITER and DEMO [1]. Therefore, one has to fully understand the damage mechanisms and erosion behavior of different PFCs upon exposure to various plasma scenarios. Furthermore, quantifying the erosion rates requires distinguishing between gross and net contributions: these can differ considerably as a large fraction of the eroded material will be locally re-deposited [1].

Tungsten (W) has proven to be a proper PFC material as demonstrated in several tokamaks like ASDEX Upgrade (AUG) [2] and JET [3]. Its main advantages are small erosion yield by plasma bombardment, good power-handling capabilities, and low accumulation of tritium in the material [4]. Re-deposition of W, for its part, is generally >50% of gross erosion [5] and approaches 100% in high-density plasmas [6].

Here, we investigate steady-state gross and net erosion of tungsten and restrict our considerations to the low-field side (outer) strike point region of the AUG. We numerically model the experimentally determined net erosion and re-deposition patterns by the ERO code [7] and by Particle-in-Cell (PIC) simulations [8], with the goal of identifying the contribution of various physical factors on the erosion characteristics. The starting point is an experiment, carried out at AUG in 2014 where W samples were exposed to a series of L-mode plasma discharges [9].

2. Review of experimental results

The experimental database comes from a dedicated experiment where special W marker samples were exposed to 13 identical plasma discharges in deuterium in the outer strike point region of AUG [9]. A full poloidal row starting from about 50 mm below the strike point, in the private flux region (PFR), and extending ~150 mm in the scrape-off layer (SOL) of the divertor plasma was covered. The location of the samples and the nominal strike line of the experiment are shown in the inset of Figure 1. All the samples had a 20-nm thick W marker on graphite as well as a shallow, 0.2 mm deep uncoated trench magnetically downstream of the marker and finally an inclined Mo marker (thickness 20 nm).

Low-density L-mode plasmas were used such that the electron temperatures around the outer strike point were 20-40 eV. The poloidal profiles of n_e and T_e, as measured by fixed Langmuir probes, are shown in Figures 2a and 2b together with their modelled counterparts that were used in subsequent ERO and PIC simulations. The net erosion of the W markers as well as re-deposition of W on the trench and on the Mo marker were determined using Rutherford backscattering spectroscopy (RBS) and the resulting erosion and deposition rates (nm/s) are collected in Figure 1.

The main observations are a noticeable net-erosion zone, coinciding with the location of the strike point, and clearly distinguishable deposition-dominated regions on both sides of the erosion maximum. On the SOL side, the deposition peak is almost 40mm wide and matches with the location of the main deposition peak of light impurities boron (B), carbon (C), and nitrogen (N) (see [9]). These observations hint towards a strong influx of material from the main chamber with a broad poloidal profile at the divertor. In the absence of direct measurements of the ion fluxes of the main impurities in the plasma (B, C, N, W) this hypothesis cannot be, however, experimentally verified.

The shape of the W re-deposition profile on the graphite and Mo markers in Figure 1 is, unexpectedly, quite similar to the profile on the W marker. By assuming graphite and Mo being efficiently shadowed from direct contact with plasma during the experiment, the deposition rate should peak close to the most prominent source, i.e., the strike point, and gradually diminish further away from it. In contrast, similar double-peak structure as for the W marker is obtained. If we now estimate the ratio between net erosion, N, and gross erosion, G, close to the strike point (and noticing that G=N+R where R stands for re-deposition), we obtain N/G~0.6-0.7. However, literature values indicate much larger re-deposition, corresponding to N/G<0.5 (see [3,6]). Thus, especially the trench and Mo marker appear to show the outcomes of multiple erosion-deposition cycles. An independent estimate for gross erosion by spectroscopic measurements of the neutral WI line at 400.9 nm supports this conclusion: a relatively sharp erosion profile with N/G=0.4-0.6 around the strike point [9].

3. Simulation setups

3.1 ERO modelling of net and gross erosion

To understand the physics behind Figure 1, we have modelled the erosion and deposition processes using ERO. ERO is a 3D Monte Carlo code that simulates the transport of test particles in the SOL [7]. We used the divertor version of the code and carried out the simulations in a box illustrated in Figure 3a. The entire toroidal (Δy=70 mm) and poloidal (Δx=300 mm) extent of the target tile were covered, and the box was Δz=50 mm high in the direction normal to the surface. A 5-mm spacing was used for the simulation grid, and in the toroidal direction periodical boundary conditions were established to prevent unphysical losses of particles. For simplicity, only the W marker was considered here and implemented in the code as bulk material. The overall simulation time was 1 s at 0.01 s steps and the number of test particles was 10^4 per time step. This was enough for equilibrium to be reached and accumulate enough statistics for reliable profiles. Losses through the poloidal and perpendicular side faces of the simulation box were generally <0.1% of the primarily sputtered atoms.

The background deuterium plasma was produced by the DIVIMP code with its Onion Skin Model (OSM, SOL option 22) activated [10]. The code returns values for the electron density, electron and ion temperatures, and flow velocity along magnetic flux surfaces of the OSM grid, which were then interpolated to obtain corresponding plasma data in the ERO simulation box. The resulting profiles for n_e and T_e along the target surface (z=0) are shown in Figures 2a and 2b together with the experimental ones. Deep in the private flux region, where the OSM background was missing, a cold plasma approximation with $n_e=10^{17}$ m^{-3} and $T_e=T_i$=0.1 eV was used. The T_e profile has a somewhat longer decay length in the SOL side and the peak is lower than what would be obtained from direct fitting into the Langmuir-probe data, while OSM solution overestimates the n_e peak at the strike point. This may have had an influence on the shape and absolute levels of the simulated erosion and deposition profiles.

In the simulations, the type and concentration of typical light impurities in the AUG divertor plasma – B, C, and N – as well as W itself originating from other parts of the torus than the simulation box were varied such that the effective charge, Z_{eff}, remained within reasonable limits (between 1.5 and 2.6) and that the concentrations of individual impurities agreed with previous measurement results from AUG, i.e., c_B, c_C, and c_N<1.0% and c_W<0.01% [11,12]. Here one should note that the measurements are from the core while in the divertor region the concentrations can locally be much larger. From coronal equilibrium [13], we obtain for the

average charge states of the impurities q_B=3, q_C=4, q_N=5, and q_W=13 in the simulation volume. The anomalous diffusion coefficient was varied from 0 to 1.0 m^2/s with $D_\perp$=0.2 m^2/s being the nominal value. No pre-calculated, integrated sputtering yields existed for the projectile-target combinations at higher charge states (q>2) to describe background plasma sputtering in terms of atoms/ion. Instead, we estimated the missing data by the Bohdansky-Yamamura formalism (see [14,15]).

The effect of **E**×**B** drift on the erosion and deposition profiles was investigated by including the electric field in the plasma background [16,17]. Since the OSM solution did not contain the electric field, nor the plasma potential, we created plausible profiles for the poloidal (E_x) and normal (E_z) components of the field by assuming the potential Φ being directly proportional to T_e, i.e,, $\Phi=3k_BT_e/e$; the electric field is then evaluated by $\mathbf{E}=-\nabla\Phi$ [18]. By assuming that the plasma potential remains the same along all the lines that are parallel with the magnetic field in the *xz* plane, one obtains a profile shown in Figure 2c.

3.2 PIC simulations

To further study the role of re-deposition on the erosion/deposition behaviour of tungsten we carried out simulations based on the magnetic sheath potentials calculated self-consistently with a PIC code introduced in [19]. Impurities were injected into the plasma as test particles and assumed not to influence the evaluated electric field as described in [8]. The required profiles for plasma parameters were again taken from the OSM solution (see Section 3.1) and also the impurity mix of the plasma was varied similarly to the case of the ERO runs.

The 2D profiles for the normal (E_z) and poloidal (E_x) components of the calculated electric field are shown in Figures 5a and 5b. The field was determined by interpolating the potentials resulting from PIC calculations for a set of parameters that include the density, the angle of the magnetic field with respect to the surface, and the ion-to-electron-temperature ratio. The component E_z reaches much larger values than E_x and what was used in ERO simulations (see Figure 2c), but only in the immediate vicinity of the surface, within the magnetic sheath; further away, the two components are comparable. Note also that the sheath electric field towards the surface extends the farthest into the plasma where the density is the highest. A correction on the potential drop was also introduced to compensate for the drift induced by the poloidal field so that ambipolarity was maintained.

Physical sputtering was treated in the simulations according to the Eckstein's formulas [20] or, in the case of B and C, to the revised Bohdansky-Yamamura formalism [14,15]. Re-deposition was computed by injecting atoms with cosine angular and Thomson energy distributions. Altogether 10^6 tungsten atoms were injected in each run and assuming at least 1000 iterations for each Larmor gyration once the particle was ionised. The simulation domain extended twice the region shown in Figures 5a and 5b, which is small in comparison to the domain spanned by ERO.

4. Results

4.1 ERO modelling

The light impurities B, C, and N are responsible for almost all the observed net erosion in the vicinity of the strike point as can be seen in Figure 3b. Here, poloidal net erosion profiles resulting from ERO simulations with c_B, c_C, and c_N ranging from 0.5% to 1.0% are shown and also the W concentration has been varied in the range c_W=0.005-0.01%. For comparison, the experimental net erosion profile of Figure 1 is reproduced in the figure. If only W was included in the simulations, net erosion would be almost two orders or magnitude smaller unless unrealistically high c_W, of the order of a few %, was used.

One should note that it is mainly the effective charge, Z_{eff}, that influences the maximum of the main erosion peak: the exact impurity composition plays a minor role. The peak scales roughly as Z_{eff}-1 within the investigated range of Z_{eff}=1.5-2.6. According to [11], the typical impurity content of the AUG SOL plasma would result in Z_{eff}~1.5-2.0, albeit Z_{eff}>2.0 can locally exist in the divertor plasmas. This leads us to select a *base case* with c_B=c_C=c_N=0.5% and c_W=0.005% for follow-up simulations, corresponding to Z_{eff}=1.81. According to Figure 3b, maximum net erosion would then be underestimated by about a factor of three. Increasing Z_{eff} improves the match but the simulated erosion rate is still off by ~25%. Besides the net-erosion peak, the simulations qualitatively predict the formation of a broad net-deposition plateau on the SOL side of the strike point, though the deposition rates are 3-5 times smaller than the experimental values. In addition, a deposition notch is seen to emerge in the PFR, just below the strike point but the remarkable narrow peak around x=-20 mm remains far from being reproduced.

The net erosion region clearly coincides with the peak of the T_e profile (see Figure 2b), while the occurrence of net deposition zones is best explained by a large fraction of the eroded particles returning on the surface somewhat off from their origin. This we can see in Figure 3c where gross erosion and re-deposition of W are illustrated for the base case along the poloidal direction. The simulated erosion and re-deposition rates are 2-5 times larger than the net-erosion rates, indicating that indeed the net/gross erosion ratio would be N/G~0.2-0.5 in contrast with N/G~0.6-0.7 reported in [9]. This gives support for the hypothesis that the measured amounts of W at the bottom of the graphite trench and on the Mo marker have been subjected to significant plasma-surface interactions during the experiment.

Besides the discrepancies discussed above, the simulated net erosion poloidally far away from the strike point approaches zero while experimentally it should saturate towards a value of ~0.04 nm/s – independent of the applied impurity content of the plasma. The reason may be due to the OSM solutions for T_e and n_e deviating from the measured profiles (see Figures 2a and 2b), which may further contribute to the erosion/deposition balance. In addition, the approximations made to obtain the missing integrated sputtering yield data (see section 3.1) may have led to underestimated gross erosion at low T_e. However, also other factors than the impurity content need to be considered.

The clearest contribution comes from the **E**×**B** drift. To this end, we ran simulations using the field profile of Figure 2c and the impurity content of the base case above. Now the net erosion peak at the strike point becomes more pronounced and the deposition maxima surrounding it more peaked such that a relatively good quantitative match with the experimental curve within the strike-zone region x=–30…20 mm is obtained. This is illustrated in Figure 4a where the resulting net erosion/deposition profiles for ERO simulations with and without the

drift are shown, together with the experimental ones. Especially, the deposition peak in the PFR has become much more noticeable than in the no-drift case of Figure 3b. This is caused purely by altered transport of the particles: gross erosion is not affected by the field but the re-deposition profile is largely shifted towards the SOL in the poloidal direction as we notice from Figure 4b. Notice, however, that both gross erosion and re-deposition remain at the same level as in Figure 3c, which sets the net/gross erosion ratio to N/G~0.5-0.6. This is close to the experimental values in [9] but still smaller and subject to large error bars induced by the shape of the electric field profile.

The normal component of the field, E_z, affects directly the distribution of W atoms on the surface by driving them poloidally either towards or away from the strike point, e.g., in the geometry of Figure 3a downwards if $E_z<0$. The other field component, E_x, influences the erosion/deposition picture only indirectly. The more negative E_x is, the more particles will drift away from the surface and migrate further before re-deposition or potential escape from the simulation, while positive values for E_x will keep the eroded atoms more tightly close to the surface.

The effect of thermal gradient forces parallel to the magnetic field [17] on the erosion/deposition profiles (not shown here) was noticed to be extremely small but cross-field diffusion played an important role in the balance between erosion and deposition. By reducing the perpendicular diffusion coefficient, net erosion and deposition peaks were both sharpened whereas larger values for $D_\perp$ efficiently re-distributed the impinging particles on the surface, thus smearing out all the prominent features of the profiles. This becomes evident from Figure 4c where the simulations at three different values ($D_\perp$=0, 0.2, and 1.0 m^2/s) are presented with the **E**×**B** drift switched on.

We conclude that the locations and magnitudes of the deposition maxima are largely attributed to the poloidal transport of particles and diffusion across the field lines. Since in our model the electric field is proportional to the gradient of the electron temperature, it is clear that even small changes in the T_e profile can result in large changes in the **E** profile, when also inaccuracies in determining the exact value for the T_e peak are taken into account. Besides, also the field component induced by parallel Pfirsch-Schlueter current would need to be taken into account [21] but this is beyond the scope of this work.

4.2 PIC modelling

In the PIC front, three simulations were performed: one with the full electric field of Figures 5a and 5b, the second with only the E_z component turned on, and the last one without any electric fields. The poloidal erosion/deposition profiles are shown in Figure 5c. Additionally, Figure 5d shows the comparison between the re-deposition and gross erosion profiles in the full electric field case.

Qualitatively, the PIC profiles have many similarities with the ERO results of Figures 3 and 4 but the net erosion maximum at the strike point is deeper and the deposition peak in the SOL side is almost non-existent. The situation without the electric field is even more extreme – only large net erosion with rates more than 2 times the experimental values. This we can understand by noting that now only Larmor gyration influences re-deposition, which will shift the entire re-deposition distribution poloidally upwards. In addition, in the very thin PIC simulation volume re-deposition remains always smaller than gross erosion, and by

combining the two effects, a peaked erosion distribution between x=–10mm and x=20mm results.

The re-deposition picture is, however, more complicated than what can be concluded from the analyses above. To this end, we separated re-deposition into two components: prompt re-deposition where tungsten ions end up on the surface within their first Larmor radius and long-range re-deposition where they undergo several gyrations before returning to the surface. The 2D re-deposition profiles are displayed in Figures 6a and 6b for both these contributions in the case E_x=0 and in Figures 6c and 6d for the full model. The case E_x=0 was considered to study transport purely in the poloidal direction. In both cases, prompt re-deposition is local, the profiles having an extent of some 10-20 mm and the effect of E_x is weak. The pattern, however, changes drastically when long-range deposition is considered. In the case E_x=0, it is mainly located poloidally downwards of the strike point and can be attributed to the **E**×**B** drift induced by large and negative E_z. This we also notice in Figure 5c: a prominent deposition peak emerges in the PFR. When the E_x component is added, however, the situation is changed: the relatively strong E_x prevents the particles from being re-deposited and drives them towards the plasma. Simultaneously, the number of particles re-deposited poloidally upwards to the strike point where E_x is oppositely oriented is strongly increased.

5. Discussion and conclusions

We have numerically modelled the experimentally determined net and gross erosion of W in the outer strike point of AUG by ERO and PIC simulations. The strong net-erosion peak at the strike point was reproduced by adding a reasonable mixture of light impurities in the plasma while the noticeable deposition peaks poloidally on both sides of the strike point could be explained by the strong **E**×**B** drift in the poloidal direction.

The determined net/gross erosion ratio was 0.2-0.6, which is to be compared with the experimentally determined value of ~0.6-0.7. The discrepancy is attributed to the re-deposited material having been in contact with plasma during the rest of the experiment. Indeed, independent, spectroscopic estimate for the net/gross erosion ratio of 0.4-0.6 support this hypothesis.

The **E**×**B** drift is the most significant individual factor contributing to the shape of the erosion/deposition profile. ERO simulations indicate that both the erosion and deposition peaks become sharper when the drift terms are activated. On the other hand, PIC simulations in the immediate neighbourhood of the samples suggest that W net erosion rate of the samples should actually be diminished and the amount of re-deposition poloidally upwards of the strike point increased by the application of the field. This demonstrates the qualitatively different balance between erosion and deposition in the sheath and further off from the surface. On top of the drifts, our results suggest a very small value for $D_\perp$ in low-density plasmas, thus cross-field diffusion playing a minor role.

The remaining shortcomings in the reproduction of the two experimentally observed deposition peaks are currently being addressed by WallDYN simulations [22] which use computational grids covering a large volume. Based on the analysis of the erosion-deposition patterns of W in medium-density L-mode plasmas, local W migration can lead to such a two-peak structure [22]. Also, our ERO simulations indicate that at least part of the observed discrepancy is caused by a loss of eroded W at the boundary of the computational grid. However, a more detailed analysis of these simulations, the preparation of background plasmas and electric-field profiles that better reproduce the n_e and T_e profiles, and the

evaluation of the missing integrated sputtering yields on the basis of data by Eckstein [19] are still pending. Finally, new experiments with modified geometry of the material samples are considered to eliminate one source of uncertainty.

Acknowledgments

This work has been carried out within the framework of the EUROfusion Consortium and has received funding from the Euratom research and training programme 2014-2018 under grant agreement number 633053. The views and opinions expressed herein do not necessarily reflect those of the European Commission. Work performed under EUROfusion WP PFC.

References

[1] G. Federici *et al.*, Nucl. Fusion **41** (2001) 1967.
[2] R. Neu *et al.*, J. Nucl. Mater. **438** (2013) S34.
[3] S. Brezinsek *et al.*, J. Nucl. Mater. **463** (2015) 11.
[4] V.Philipps, J. Nucl. Mater. **415** (2011) S2.
[5] A. Chankin *et al.*, Plasma Phys. Control. Fusion **56** (2014) 025003.
[6] R. Neu *et al.*, Plasma Phys. Control. Fusion **53** (2011) 124040.
[7] A. Kirschner *et al.*, Nucl. Fusion **40** (2000) 989.
[8] N. Mellet *et al.*, Phys. Scr. **T167** (2016) 014064.
[9] A. Hakola *et al.*, Phys. Scr. **T167** (2016) 014026.
[10] http://starfire.utias.utoronto.ca/divimp/docs/divdocs.html (ref. 10.05.2016).
[11] A. Kallenbach *et al.*, Nucl. Fusion **49** (2009) 045007.
[12] T. Eich *et al.*, J. Nucl. Mater. **438** (2013) S72.
[13] https://www-amdis.iaea.org/FLYCHK/ (ref. 10.05.2016).
[14] C. Garcia-Rosales *et al.*, J. Nucl. Mater. **218** (1994) 8.
[15] Y. Yamamura *et al.*, IPPJ-AM-26, Nagoya (1983).
[16] L. Aho-Mantila *et al.*, Nucl. Fusion **52** (2010) 103006.
[17] L. Aho-Mantila *et al.*,Nucl. Fusion **52** (2010) 103007.
[18] P. C. Stangeby, *The Plasma Boundary of Magnetic Fusion Devices*, IOP Publishing Ltd., 2000
[19] J. P. Gunn, Phys. Plasmas **4** (1997) 4435.
[20] W. Eckstein, Sputtering by Particle Bombardment (Topics in Applied Physics vol. 110) (Springer Berlin Heidelberg) (2007) 33.
[21] I. Senichenkov *et al.*, Europhysics Conference Abstracts **39E** (2015) P5.191.
[22] G. Meisl *et al.*, Nucl. Fusion **56** (2016) 036014.

Figure captions

Figure 1. Experimentally determined poloidal net deposition/erosion profile of the W marker as well as poloidal re-deposition profiles for W on the graphite and Mo markers. Negative values denote net erosion, positive net deposition and PFR corresponds to the poloidal distance being negative. Inset shows schematic illustration of the AUG divertor, target tile (red), and marker samples used in the 2014 erosion experiment. At the divertor, the magnetic field points towards the viewer.

Figure 2. (a,b) Experimental Langmuir-probe data and simulated OSM profiles for the poloidal profiles of (a) electron density and (b) electron temperature around the strike point. (c) Poloidal profiles for the two electric field components (E_x and E_z) used in the ERO simulations together with the definitions for the ERO co-ordinate system.

Figure 3. (a) Definition of the ERO simulation box and the applied co-ordinate system. (b) ERO results for the poloidal net deposition/erosion profile in the base case (blue, c_W=0.005%, c_B=c_C=c_N=0.5%) and with c_W=0.01%, c_B=c_C=c_N=0.5% (red) and c_W=0.01%, c_B=c_C=c_N=1.0% (black). Also the experimental profile has been reproduced. (c) Poloidal gross erosion (blue) and re-deposition (red) profiles for the base case.

Figure 4. (a) ERO results for the poloidal net deposition/erosion profile in the base case both with (red) and without (blue) the electric field. (b) Poloidal gross erosion (blue) and re-deposition (red) profiles for the case with the electric field being switched on. (c) Influence of cross-field diffusion on net deposition/erosion: $D_\perp$=0 (black), $D_\perp$=0.2m^2/s (red), and $D_\perp$=1.0m^2/s (orange). In (a) and (c) also the experimental profile has been reproduced.

Figure 5. (a,b) 2D profiles for (a) E_z and (b) E_x used in the PIC simulations. The field had been generated by interpolating the magnetic sheath potentials calculated by the PIC code. (c,d) PIC results for (c) net deposition/erosion computed using the test-particle in three cases: no electric field (blue), only the E_z component activated (blue) and the full electric field (black) and (d) poloidal gross erosion (blue) and deposition (red) profiles in the full electric field case.

Figure 6. PIC results for 2D re-deposition profiles of the prompt (a,c) and long-range (b,d) fractions. Two models have been compared: only E_z (a,b) and the full electric field (c,d).

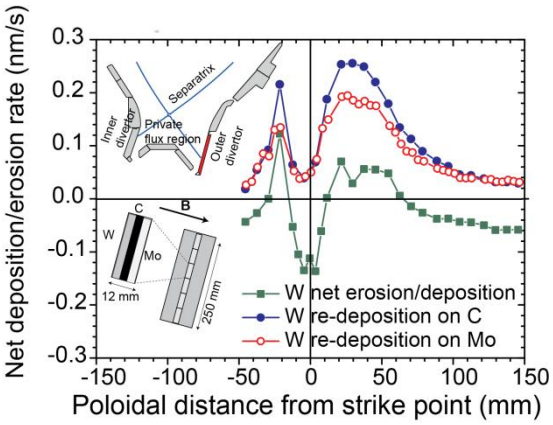

Figure 1.

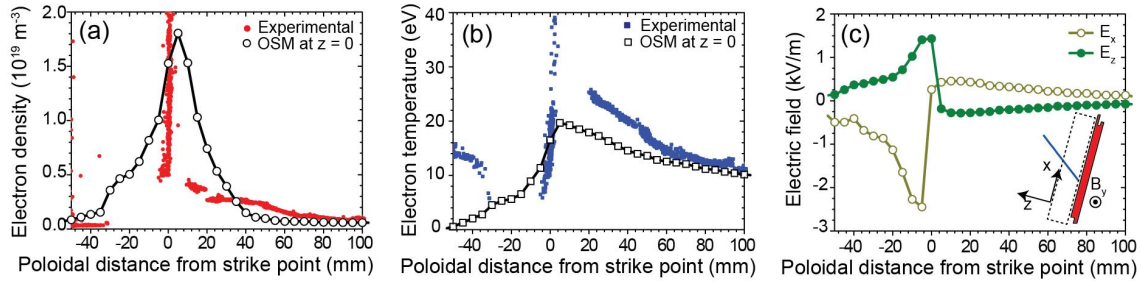

Figure 2.

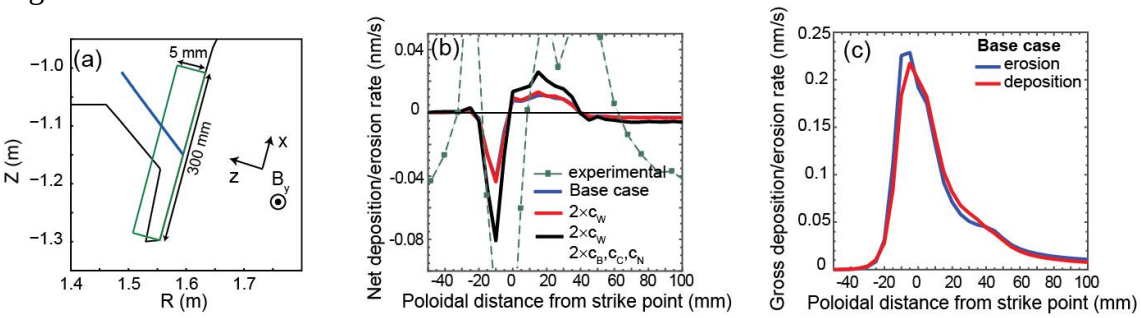

Figure 3.

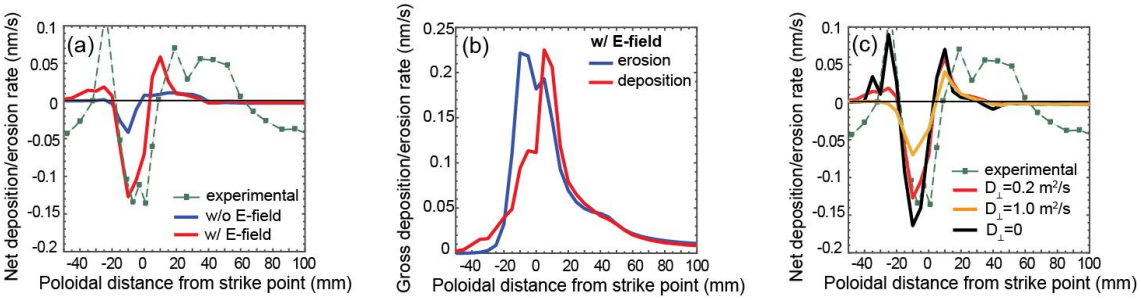

Figure 4.

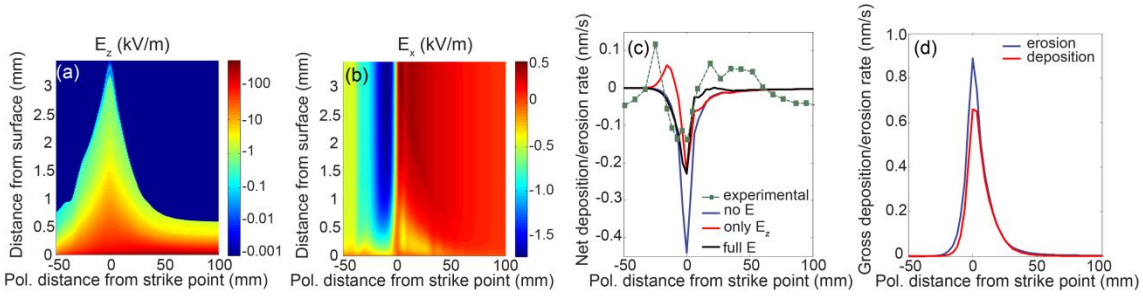

Figure 5.

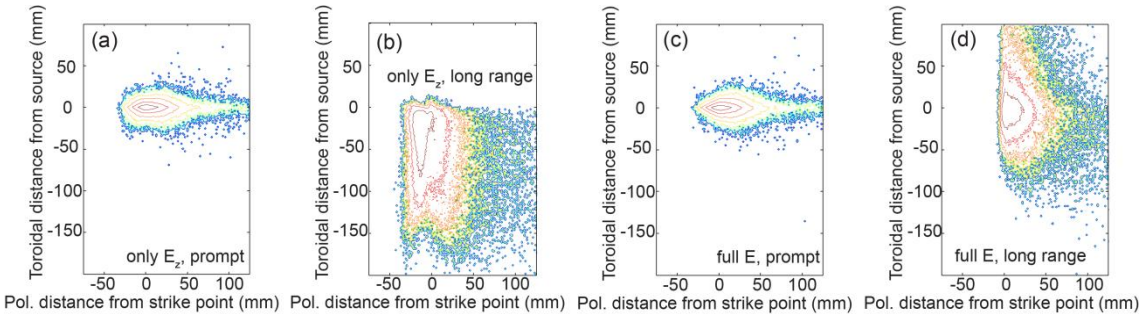

Figure 6.